

# From Quantum Chaos to a Reversed Quantum Disentangled Liquid in a Disorder-Free Spin Ladder

Hanieh Najafzadeh\* and Abdollah Langari†

*Department of Physics, Sharif University of Technology, Tehran 1458889694, Iran*

The mechanisms by which isolated interacting quantum systems evade thermalization extend beyond disorder-induced many-body localization, encompassing a growing class of interaction-driven phenomena. We investigate a spin- $\frac{1}{2}$  ladder with asymmetric XY leg couplings and tunable Ising interactions on the rungs, and identify the microscopic origin of many-body localization (MBL) in this setting. Through a suite of diagnostics—including entanglement dynamics, fidelity susceptibility, adiabatic gauge potential norms, level-spacing statistics and entropy of eigenstates—we uncover a reentrant progression of dynamical regimes as the rung coupling  $J_z$  is varied: integrable behavior at  $J_z = 0$ , quantum chaos at intermediate  $J_z$ , and a robust nonthermal regime at strong coupling. In the latter regime, we demonstrate the emergence of a *reversed quantum disentangled liquid* (reversed-QDL), where the light species thermalizes while the heavy species remains localized. The strong-coupling limit further yields emergent local integrals of motion anchored in a fixed-point structure, providing a microscopic origin of the observed quasi-MBL dynamics. These results establish reversed-QDL as a distinct, disorder-free route to nonergodicity and broaden the classification of dynamical phases in quantum matter.

## I. INTRODUCTION

The breakdown of thermalization in isolated quantum systems has emerged as a central topic in nonequilibrium many-body physics. While generic interacting systems are expected to thermalize according to the eigenstate thermalization hypothesis (ETH) [1–4], exceptions to this rule—such as many-body localization (MBL) in disordered systems [5–10]—have revealed the rich landscape of nonergodic quantum phases. More recently, attention has shifted toward disorder-free mechanisms of thermalization failure, including Hilbert space fragmentation [11–14], quantum many-body scars [15–18], mixed-phase space [19], Stark-MBL [20, 21] and quantum disentangled liquids (QDLs) [22].

QDLs represent a class of nonthermal states in which subsystems with different dynamical scales decouple entanglement-wise: typically, a “heavy” species thermalizes while a “light” species remains localized. Originally proposed in systems with mass imbalance or internal constraints, QDLs provide a framework for understanding partial ergodicity in constrained quantum dynamics [22–25]. In parallel, quasi-many-body localization (quasi-MBL)—characterized by slow entanglement growth and long-lived memory retention in the absence of quenched disorder—has been observed in spin ladders and other constrained, disorder-free settings [26–31]. We stress that by quasi-MBL we refer to disorder-free, finite-size localization-like dynamics, which are distinct from true MBL driven by randomness.

While Hilbert-space fragmentation and quantum many-body scars also represent disorder-free mechanisms of nonergodicity, their microscopic origins are fundamen-

tally distinct from the scenario studied here. Fragmentation arises from exactly preserved subspaces that confine dynamics [32], while scars correspond to atypical eigenstates embedded in an otherwise thermal spectrum [33]. By contrast, our mechanism is rooted in emergent local integrals of motion (LIOMs) [34, 35] that originate from the strong-coupling fixed point, where the integrals of motion are determined by the rung configurations. At this fixed point, the dynamics are effectively frozen by the dominance of the inter-leg coupling, and the system admits a set of integrals of motion. For large but finite  $J_z$ , these LIOMs remain quasi-conserved, giving rise to slow dephasing and logarithmic entanglement growth characteristic of reversed-QDL dynamics. Moreover, the reversed-QDL regime identified in this work reflects an inverted entanglement hierarchy between dynamical species, a feature absent in both fragmentation and scarred dynamics. Our results therefore establish a conceptually distinct and complementary route to disorder-free nonergodicity.

Despite these advances, the microscopic mechanism underlying quasi-MBL in such systems remains poorly understood. In this work, we address this question in a spin- $\frac{1}{2}$  ladder model featuring XY interactions along the legs and tunable Ising couplings across the rungs (see Fig. 1). We perform a comprehensive numerical analysis using complementary diagnostics, including entanglement dynamics [36, 37], fidelity susceptibility [38–41], adiabatic gauge potential (AGP) norms [42–45], and level-spacing statistics [6, 46, 47]. In the presence of (effective) mass imbalance, we reveal a reentrant structure in the system’s thermalization behavior as a function of the rung coupling: the ladder evolves from an integrable, nonergodic regime to a chaotic ETH-consistent phase, and ultimately enters a robust nonthermal regime at strong coupling.

Remarkably, we identify the latter regime as a *reversed quantum disentangled liquid*, in which the light

\* hanieh.najafzadeh@sharif.edu

† langari@sharif.edu

species thermalize while the heavy ones remain localized—reversing the entanglement hierarchy observed in conventional QDLs. This behavior uncovers the microscopic mechanism for quasi-MBL in translation invariant systems and establishes a two-scenario framework for the emergence of nonergodic dynamics without disorder. Our findings broaden the landscape of thermalization failure in many-body systems and point toward a novel class of stable, interaction-induced nonergodic phases.

Previous works have shown that disorder is not strictly necessary to induce localization. Instead, interactions in translation-invariant systems—particularly in spin ladders—can give rise to quasi-MBL, characterized by anomalously slow entanglement growth and long-lived memory [26–31]. However, these studies primarily focused on phenomenological features and prethermal behavior, without uncovering the mechanism responsible for long-time localization-like dynamics. In this work, we move beyond phenomenological descriptions and provide a systematic diagnostic of thermalization and localization dynamics in the ladder model. Our central goal is to uncover the physical mechanism underlying the quasi-MBL behavior observed in Fig. 2, and to demonstrate how it arises purely from interaction asymmetry and coupling structure.

Section II introduces the model, while Sec. III outlines its dynamical properties. In Sec. IV, we present extensive numerical simulations that characterize the distinct regimes of the model. Section V is devoted to elucidating the mechanism of reversed-QDL behavior and its relation to the strong-coupling limit. Finally, Sec. VI summarizes our findings and discusses their broader implications.

## II. MODEL

We consider a spin- $\frac{1}{2}$  two-leg ladder composed of  $L$  rungs as shown in Fig. 1, where each rung consists of two spins corresponding to the lower ( $\tau$ ) and upper ( $\sigma$ ) ones, respectively [26]. The system is governed by the following Hamiltonian assuming periodic boundary conditions (PBC, i.e.  $\sigma_{L+1} = \sigma_1, \tau_{L+1} = \tau_1$ ) along legs,  $H = H_\tau + H_\sigma + H_{zz}$ , where

$$\begin{aligned} H_\tau &= J \sum_{i=1}^L (\tau_i^x \tau_{i+1}^x + \tau_i^y \tau_{i+1}^y), \\ H_\sigma &= J' \sum_{i=1}^L (\sigma_i^x \sigma_{i+1}^x + \sigma_i^y \sigma_{i+1}^y), \\ H_{zz} &= J_z \sum_{i=1}^L \tau_i^z \sigma_i^z, \end{aligned} \quad (1)$$

where  $\tau_i^\alpha$  and  $\sigma_i^\alpha$  ( $\alpha = x, y, z$ ) are Pauli operators acting on site  $i$  of the lower and upper legs, respectively. The coupling  $J_z$  introduces the strength of Ising interaction on each rung. The intra-leg XY interactions act with strength  $J$  on the lower leg and  $J'$  on the upper leg [48].

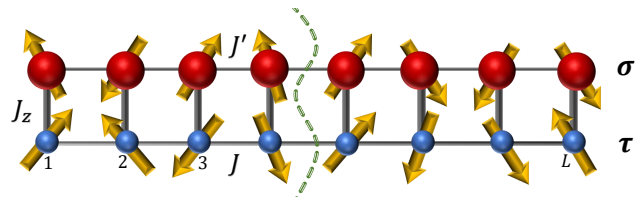


FIG. 1. (Color online) Schematic illustration of the two-leg spin- $\frac{1}{2}$  ladder model. Blue and red spheres denote spins on the lower ( $\tau$ ) and upper ( $\sigma$ ) legs, respectively, which are coupled via XY interactions  $J$  and  $J'$ . Rung couplings  $J_z$  introduce inter-leg Ising interactions. The dashed green line denotes the bipartition used to measure entanglement entropy.

We fix  $J = 1$  to define the energy scale,  $J' = 0.001$  and explore the physics as a function of the inter-leg coupling  $J_z$ , focusing on the strongly asymmetric regime  $J' \ll J$ . This limit induces a strong asymmetry in dynamical timescales between the two legs, enabling partial thermalization and nontrivial entanglement structures—key ingredients for QDL or quasi-MBL physics—which is going to be uncovered in this article.

It would be interesting to mention that the XY Hamiltonian of each leg can be mapped to a spinless free fermion model via a Jordan-Wigner transformation [49, 50]. Let us define  $c_\ell^\dagger$  ( $c_\ell$ ) as the creation (annihilation) of a fermion on site  $\ell$  on the lower leg and the corresponding ones on the upper leg as  $\tilde{c}_\ell^\dagger$  ( $\tilde{c}_\ell$ ). According to the Jordan-Wigner transformation the Pauli operators on the lower leg are defined by

$$\begin{aligned} \tau_\ell^+ &= c_\ell^\dagger e^{(i\pi \sum_{j<\ell} n_j)}, \\ \tau_\ell^- &= e^{(-i\pi \sum_{j<\ell} n_j)} c_\ell, \\ \tau_\ell^z &= 2(n_\ell - \frac{1}{2}), \quad n_\ell = c_\ell^\dagger c_\ell. \end{aligned} \quad (2)$$

An analogous mapping is defined between the Pauli operators  $\sigma$  and the fermions  $\tilde{c}_\ell^\dagger, \tilde{c}_\ell$  (on the upper leg including a Klein factor), where  $\{c, \tilde{c}\} = 0$ . The Hamiltonian of the ladder will be written in terms of fermion operators as

$$\begin{aligned} H_\tau &= 2J \sum_{\ell=1}^L (c_\ell^\dagger c_{\ell+1} + c_{\ell+1}^\dagger c_\ell), \\ H_\sigma &= 2J' \sum_{\ell=1}^L (\tilde{c}_\ell^\dagger \tilde{c}_{\ell+1} + \tilde{c}_{\ell+1}^\dagger \tilde{c}_\ell), \\ H_{zz} &= 4J_z \sum_{\ell=1}^L n_\ell \tilde{n}_\ell - 2J_z \sum_{\ell=1}^L (n_\ell + \tilde{n}_\ell) + const. \end{aligned} \quad (3)$$

The fermion representation of Hamiltonian (3) shows that the ladder is composed of two free fermion chains coupled via density-density interaction between aligned sites across each rung. It has been mentioned in [26] that for  $J' = 0$ , the density of fermions on the upper chain (or equivalently the spin configurations of  $\sigma$ 's) plays the role of a quenched disorder for the lower chain fermions,

leading to (single particle) Anderson localization [51] at strong disorder. Upon taking into account the effect of small  $J'$  ( $J' \ll J$ ), the slow dynamics of heavy fermions ( $\tilde{c}$ ) could act as slow variation of disorder landscape in an interacting fermion system. The long-time dynamics of the model shows a slow decay of polarization [26, 52], which mimics an MBL-like dynamics dubbed quasi-MBL regime. The signature of the latter phase is decoded in the slow (logarithmic) growth of entanglement entropy as shown in Fig. 2 for large Ising coupling ( $J_z = 10, 20$ ). We are going to uncover the mechanism of slow dynamics and investigate the effect of Ising interaction on the dynamical behavior of the model within several diagnostics approaches.

### III. ENTANGLEMENT DYNAMICS

Entanglement entropy measures how strongly two parts of a quantum system are quantum-correlated, which is a universal probe of quantum structure, dynamics, and phases of matter [53, 54]. More specifically, the dynamical behavior of entanglement entropy gives a clear signature of the dynamical properties of the phase of system. In a thermal system (which obeys ETH or being in a chaotic phase), the entanglement entropy grows rapidly with time (typically ballistically, i.e. linear in time for 1D systems) and eventually saturates to a volume law value [3, 4]. While in an MBL phase, entanglement entropy grows logarithmically in time and saturates to a subthermal volume law (much smaller than in the thermal phase) [36].

For a pure state,  $|\psi(t)\rangle$ , the density matrix is given by  $\rho(t) = |\psi(t)\rangle\langle\psi(t)|$  as the state evolves via the unitary evolution of the Hamiltonian (Eq. 1). We compute the bipartite entanglement entropy,

$$S_{\text{ent}}(t) = -\text{Tr}_A \rho_A \log \rho_A, \quad (4)$$

where  $\rho_A$  is the reduced density matrix obtained by tracing out half of the system across a central vertical cut (dashed line in Fig. 1), i.e.,  $\rho_A = \text{Tr}_B(\rho)$ . The time evolution starts from an initial state, which is random product states sampled uniformly from the Hilbert space, and observables are averaged over 100 such realizations to suppress fluctuations. Time evolution is performed via exact diagonalization of the full Hamiltonian. As shown in Fig. 2, the dynamics of averaged half-cut entanglement entropy  $S_{\text{ent}}(t)$  exhibits distinct behavior as a function of the inter-leg coupling  $J_z$ , for  $J = 1, J' = 0.001$ . In the strongly interacting regime ( $J_z \gg 1$ ),  $S_{\text{ent}}(t)$  shows a rapid initial rise due to the dynamics of  $\tau$  degrees of freedom followed by a broad saturation-like plateau, which begins at  $t_1 \sim (J)^{-1}$  and ends at  $t_2 \sim (J')^{-1}$  [26]. Beyond this regime, the entanglement grows slowly and logarithmically (with smaller slope) in time—a hallmark of non-thermalizing phase in translation-invariant systems. The latter regime ( $t > t_3$ ) is responsible for a residual memory in a finite system before diminishing, however,

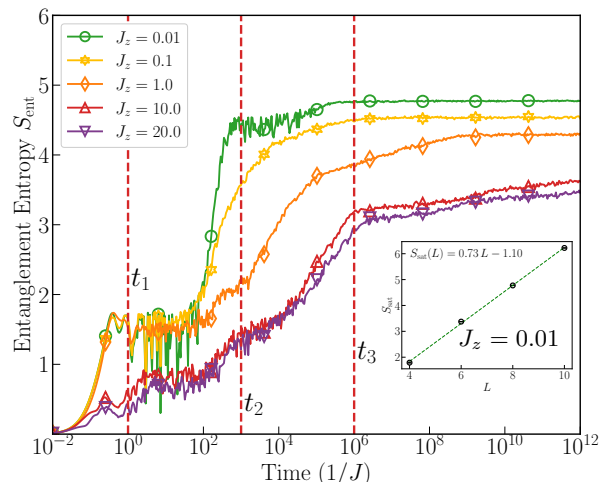


FIG. 2. (Color online) Time evolution of the half-cut entanglement entropy  $S_{\text{ent}}(t)$  for various values of inter-leg Ising coupling  $J_z$ , computed for a spin-1/2 ladder of size  $L = 8$  with periodic boundary conditions and  $J' = 0.001$ . The system exhibits a crossover from rapid thermalization at weak coupling ( $J_z \ll 1$ ) to slow, logarithmic growth characteristic of quasi-many-body localization ( $J_z \gg 1$ ). For  $J_z = 10$ , the labeled times  $t_1$ ,  $t_2$  and  $t_3$  respectively mark the rapid rise due to local interactions, the onset and crossover to the logarithmic growth regime, highlighting the separation of dynamical timescales inherent to quasi-MBL. (**Inset**) The entropy saturation value plotted against system size at  $J_z = 0.01$  demonstrates a clear volume-law scaling, supports the identification of a chaotic phase.

the diminishing time scales with system size to infinity, according to the analysis presented in Ref. [26]. The presence of this logarithmic regime at late times, which starts at  $t_3$ , reflects the emergence of a slow dephasing process across the ladder, driven solely by interaction-induced constraints.

In contrast, for weak inter-leg coupling ( $J_z \ll 1$ ), the entanglement dynamics grows fast and reaches its saturation value. However, it reveals an additional plateau close to saturation at intermediate times, which ends before  $t_3 \sim (J'^2/J_z)^{-1}$  [26]. The appearance of this second plateau indicates that thermalization is enhanced within the fast leg—mediated by its interaction with the slow leg—before global dephasing occurs. This behavior signals more structured, multi-stage dynamics at small  $J_z$ . Consistent with this picture, the inset of Fig. 2 shows that the saturation value at  $J_z = 0.01$  scales linearly with system size, i.e. it obeys a clear volume law. This scaling behavior provides direct evidence that the weak-coupling regime is chaotic and thermalizing, in sharp contrast to the logarithmic entanglement growth and sub-volume saturation characteristic of the quasi-MBL regime at large  $J_z$ .

#### IV. OBSERVABLES AND DIAGNOSTICS

To characterize the emergent phases of the spin ladder model defined in Sec. III, we employ a set of complementary observables to distinguish between thermal and nonthermal regimes across different coupling strengths  $J_z$ .

##### A. Fidelity susceptibility and adiabatic gauge potential norm

The fidelity susceptibility (FS), defined as the diagonal component of the quantum geometric tensor with respect to a coupling parameter  $\lambda$ , provides a sensitive probe of the structure of eigenstates [38, 55]. For the  $n$ -th eigenstate  $|\psi^{(n)}\rangle$ , i.e.  $H|\psi^{(n)}\rangle = E_n|\psi^{(n)}\rangle$ , the fidelity susceptibility is expressed as

$$\chi_n = \sum_{m \neq n} \frac{|\langle \psi^{(n)} | \partial_\lambda H | \psi^{(m)} \rangle|^2}{(E_m - E_n)^2}, \quad (5)$$

quantifying the response of  $|\psi^{(n)}\rangle$  to an infinitesimal change in  $\lambda$ . Since the denominator involves squared energy differences,  $\chi_n$  is exponentially sensitive to the fine structure of the many-body spectrum, making it a natural diagnostic of ergodic versus localized behavior [39–41, 43]. Therefore, fidelity susceptibility is a valuable tool for illustrating how dynamical behavior changes between different regimes.

Since all eigenstates may contribute to the dynamics, it is natural to consider the fidelity susceptibility (FS) averaged over the spectrum. In order to capture the scaling behavior while reducing the effect of large eigenstate-to-eigenstate fluctuations, it is more convenient to analyze the typical value of  $\chi_n$  obtained by averaging its logarithm [39, 43, 44]. We thus define the *typical fidelity susceptibility* as

$$\chi_{\text{typ}} = e^\zeta; \quad \zeta = \langle \log(\chi_n) \rangle, \quad (6)$$

where  $\langle \dots \rangle$  denotes averaging over different eigenstates, within each symmetry sector. This log-average suppresses the influence of rare resonances while retaining the exponential sensitivity of the probe, making  $\zeta$  particularly useful for distinguishing between ETH (chaotic), integrable, and MBL phases through their different scaling behaviors [44, 56].

In order to investigate the effect of the rung coupling  $J_z$  on the dynamics of our model, we set the driving parameter to be  $\lambda = J_z$ . This choice leads to

$$\partial_\lambda H \equiv \frac{1}{L} \sum_{\ell=1}^L \tau_\ell^z \sigma_\ell^z \quad (7)$$

which is the operator entering the calculation of  $\chi_n$  in Eq. 5. For each symmetry sector  $\theta$  with dimension  $D_\theta$ ,

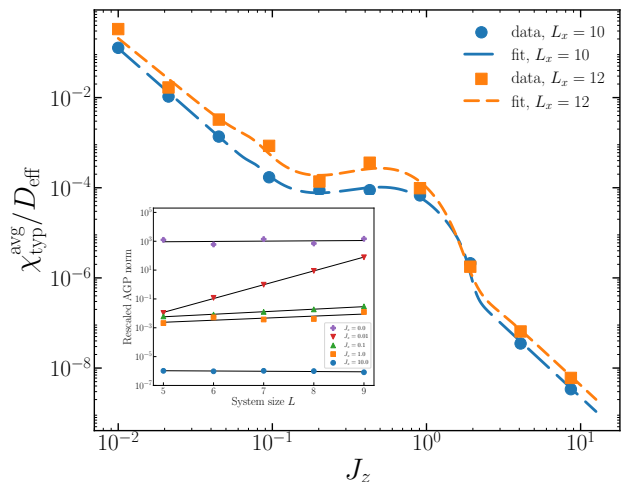


FIG. 3. (Color online) Dimension-weighted average of fidelity susceptibility  $\chi_{\text{typ}}^{\text{avg}}/D_{\text{eff}}$  as a function of  $J_z$  for ladder lengths  $L = 10, 12$ . A clear peak appears near  $J_z \simeq 1$ , signaling a dynamical crossover. (Inset) Rescaled AGP norm  $\|A_\lambda\|^2/L$  as a function of system size for different values of  $J_z$  on a logarithmic scale. For  $J_z = 0$  (integrable case), the scaling of  $\|A_\lambda\|^2$  is linear in  $L$ , while for small nonzero  $J_z$  values the norm grows exponentially, with  $J_z = 0.01$  showing clear chaotic behavior. Near  $J_z \simeq 1$ , deviations from exponential scaling appear, and for larger  $J_z$ , the exponential growth is strongly reduced. The AGP results are computed in the total-magnetization sector  $S_{\text{tot}}^z = 0$  and averaged over all  $(k, \mathcal{Z})$  symmetry sectors.

we compute the sector-resolved fidelity-susceptibility and form a dimension-weighted average

$$\chi_{\text{typ}}^{\text{avg}}(J_z) = \frac{\sum_{\theta} D_{\theta} \chi_{\text{typ}}^{(\theta)}(J_z)}{\sum_{\theta} D_{\theta}}. \quad (8)$$

In Fig. 3 we present,  $\chi_{\text{typ}}^{\text{avg}}/D_{\text{eff}}$ , as a function of  $J_z$  for different ladder lengths  $L$ , where  $D_{\text{eff}}$  is the mean of the Hilbert space dimensions of all considered symmetry sectors. A pronounced peak is observed near  $J_z \simeq 1$  for  $L = 10, 12$ , which provides clear evidence of a dynamical crossover between two regimes [39, 43]. Due to the strong finite-size effects, however, it is not possible to reliably extract a universal scaling function from the available data for the fidelity susceptibility.

All fidelity-susceptibility results are computed in the symmetry-resolved sector  $\theta : (S_{\tau}^z, S_{\sigma}^z, k, \mathcal{Z}) = (0, 0, k_m, \pm 1)$  via the shift-and-invert method, focusing on the central region of the spectrum—capturing approximately 50% of the states for  $L = 10$  and 10% for  $L = 12$ . Here  $S_{\tau}^z$  and  $S_{\sigma}^z$  denote the total magnetizations on the two legs,  $k_m = 2\pi m/L$  is the lattice momentum and  $\mathcal{Z}$  specifies the spin-inversion symmetry. The data of Fig. 3(main) is averaged over all non-reflection-symmetric momentum sectors ( $k_m \neq 0, \pi$ ) for  $L = 10$  and over four generic momentum sectors for  $L = 12$ , namely  $(0, 0, \pi/3, \pm 1)$  and  $(0, 0, 5\pi/6, \pm 1)$ .

The adiabatic gauge potential (AGP) quantifies the generator of slow deformations in parameter space [42, 57]. Its Hilbert–Schmidt (Frobenius) norm coincides with the eigenstate-averaged fidelity susceptibility [43]. We evaluate the AGP with respect to the rung coupling  $\lambda = J_z$  and use the regularized norm

$$\|A_\lambda\|^2 = \frac{1}{\mathcal{D}} \sum_n \sum_{m \neq n} \frac{\omega_{mn}^2 |\langle \psi^{(m)} | \partial_\lambda H | \psi^{(n)} \rangle|^2}{(\omega_{nm}^2 + \mu^2)^2}, \quad (9)$$

with  $\omega_{mn} = E_m - E_n$ ,  $\mathcal{D}$  the Hilbert-space dimension, and cutoff  $\mu = L\mathcal{D}^{-1}$  chosen to suppress the zero-frequency divergence [43, 45].

*Expected scaling.*— The AGP norm tracks many-body complexity [43]. In ergodic/ETH regimes one expects entropy-controlled growth,  $\|A_\lambda\|^2 \propto e^{S(L)}$ , with  $S(L) \simeq sL$  and  $s = \ln 4$  for our two-leg spin- $\frac{1}{2}$  ladder. In the free noninteracting limit the AGP is quasi-local and extensive,  $\|A_\lambda\|^2 \propto L$ . Generic integrable or weakly chaotic regimes exhibit sub-ETH behavior,  $\|A_\lambda\|^2 \propto L^\beta$  ( $\beta > 1$ ) or  $\|A_\lambda\|^2 \propto e^{\alpha S(L)}$  with  $0 < \alpha < 1$ .

The inset of Fig. 3 shows the rescaled norm  $\|A_\lambda\|^2/L$  versus  $L$  on a logarithmic axis. Fitting  $\ln(\|A_\lambda\|^2/L) = \alpha(J_z)L + \text{const.}$  over  $L = 5, \dots, 9$  yields  $\alpha = \{0.050, 2.207, 0.405, 0.329, 0.043\}$  for  $J_z = \{0, 10^{-2}, 10^{-1}, 1, 10\}$ , so  $\|A_\lambda\|^2/L \sim e^{\alpha(J_z)L}$ . so that compactly  $\|A_\lambda\|^2/L \sim e^{\alpha(J_z)L}$ .

These values align with the theoretical picture mentioned above. Unlike the FS, the AGP norm is a frequency-filtered and regularized spectral quantity, making it explicitly sensitive to how near-resonant level pairs contribute as the many-body level spacing decreases with increasing system size. As a result, the AGP norm naturally exhibits distinct size scaling for different values of  $J_z$ , reflecting qualitative differences between ETH-like and non-ergodic regimes.

Distinguishing a mild exponential from a power law over  $L = 5, \dots, 9$  is intrinsically difficult; nevertheless, the intermediate couplings display clear ETH-like exponential scaling tied to the entropy density  $s = \ln 4$ , whereas both integrable edges ( $J_z = 0$  and large  $J_z$ ) remain strongly suppressed.

## B. Entropy of eigenstates

The final quantity we compute to probe the dynamical behavior is the normalized average entropy [58],

$$S_{\text{avg}} = \frac{1}{\mathcal{D}} \sum_n \frac{S_A^{(n)}}{2L_A \ln 2}, \quad (10)$$

where  $\mathcal{D}$  is the total Hilbert-space dimension and  $S_A^{(n)}$  denotes the half-cut entanglement entropy of the eigenstate  $|\psi^{(n)}\rangle$ , as defined in Eq. (4). Here  $L_A$  is the size

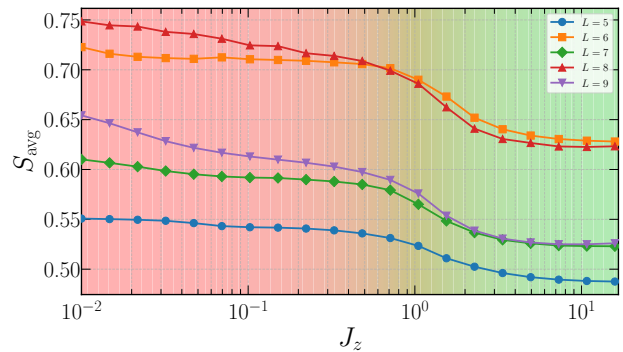


FIG. 4. (Color online) Normalized average entropy  $S_{\text{avg}}$  versus  $J_z$  for system sizes  $L = 5, 6, 7, 8, 9$ . For  $J_z < 1$ , larger values of  $S_{\text{avg}}$  indicate full Hilbert-space exploration in the chaotic phase, while for  $J_z > 1$ , a marked decrease signals localization, consistent with a dynamical crossover near  $J_z \simeq 1$ . Slight differences between odd and even  $L$  arise from the bipartition asymmetry in entropy calculations.

(number of rungs) of the subsystem  $A$  used in the bipartition. For even  $L$  we set  $L_A = L/2$ , while for odd  $L$  we take  $L_A = (L + 1)/2$ .

We plot  $S_{\text{avg}}$  over 80% of the central spectrum as a function of  $J_z$  for system sizes  $L = 5, 6, 7, 8, 9$  in Fig. 4. The data exhibit two distinct regimes: for  $J_z < 1$ ,  $S_{\text{avg}}$  takes larger values, indicating full access to the Hilbert space consistent with a chaotic phase; for  $J_z > 1$ ,  $S_{\text{avg}}$  decreases clearly, signaling non-ergodicity in the Hilbert space. This behavior aligns with other numerical diagnostics that is a supporting indicator for dynamical crossover around  $J_z \simeq 1$ .

It is also worth noting that results for odd and even system sizes differ slightly. This discrepancy arises from the bipartition cut used in calculating the entanglement entropy, which is symmetric for even  $L$  but asymmetric for odd  $L$ .

We have also computed the mean level spacing as a function of  $J_z$  (see Appendix A), which demonstrates the crossover from Gaussian statistics at small  $J_z$  to Poisson-type statistics for large  $J_z$ , consistent with the other diagnostics.

## V. MECHANISM OF QUANTUM DYNAMICS

All quantum diagnostics discussed so far indicate that the spin ladder described by the Hamiltonian in Eq. 1 exhibits three distinct dynamical phases/regimes as a function of  $J_z$ . At  $J_z = 0$ , the model consists of two decoupled integrable spin- $\frac{1}{2}$  chains. Introducing a small but finite  $J_z$  drives the system into a chaotic phase, which persists up to  $J_z \lesssim 1$ , where a dynamical crossover occurs. For  $J_z \gtrsim 1$ , the model exhibits quasi-MBL behavior, as summarized in the diagram shown in Fig. 7.

Despite the absence of disorder, this translation-

ally invariant system displays logarithmic entanglement growth, reminiscent of conventional MBL phases. Due to the strong asymmetry in the XY couplings along the two legs ( $J' \ll J$ ), the system may also be interpreted as a quantum disentangled liquid (QDL): the heavier  $\sigma$ -spins thermalize rapidly and effectively localize the lighter  $\tau$ -spins, preventing their full thermalization. This interplay leads to the slow, logarithmic growth of entropy. In the following, we aim to uncover the underlying mechanism responsible for the quasi-MBL behavior observed at large  $J_z$ .

### A. Measured Entanglement Entropy: QDL Diagnostic

To probe the structure of partial thermalization, we compute the *measured entanglement entropy*, a diagnostic originally introduced in the context of quantum disentangled liquids (QDLs) [22, 25, 59]. In our setup, we treat the  $\sigma$  spins as the measured subsystem, and examine the entanglement properties of the  $\tau$  spins after projective measurements are performed on the  $\sigma$  spins.

Given an energy  $E_m$  and its corresponding eigenstate  $|\psi^{(m)}\rangle$  of the Hamiltonian in Eq. (1), we express it in the product basis of  $\tau$  and  $\sigma$  spins as

$$|\psi^{(m)}\rangle = \sum_{i,j} C_{ij}^{(m)} |\mu_i^{(\tau)}\rangle \otimes |\eta_j^{(\sigma)}\rangle, \quad (11)$$

where  $|\mu_i^{(\tau)}\rangle$  and  $|\eta_j^{(\sigma)}\rangle$  form complete basis sets for the  $\tau$  and  $\sigma$  spins, respectively.

Upon performing a projective measurement on the  $\sigma$  spins in the computational (i.e.,  $z$ )-basis, the probability of obtaining the  $j$ -th configuration ( $|\eta_j^{(\sigma)}\rangle$ ) in  $\sigma$ -Hilbert space is

$$P_j^{(m)} = \sum_i |C_{ij}^{(m)}|^2. \quad (12)$$

A schematic illustration is given in the inset-(a) of Fig. 5, where the  $\sigma$  configuration is fixed after the projection and is shown with grey color, while the linear combination of the  $\tau$  degrees of freedom define the projected state. The resulting projected state on the  $\tau$  spins becomes

$$|\psi_j^{(m)}\rangle = \frac{1}{\sqrt{P_j^{(m)}}} \sum_i C_{ij}^{(m)} |\mu_i^{(\tau)}\rangle, \quad (13)$$

where the subscript  $j$  stands for the  $j$ -th configuration of  $\sigma$  spins. We then partition the  $\tau$  spins into two equal spatial regions  $A$  and  $B$ , and compute the reduced density matrix of region  $A$  by tracing out  $B$ :

$$\rho_A^{(m,j)} = \text{tr}_B \left[ |\psi_j^{(m)}\rangle \langle \psi_j^{(m)}| \right]. \quad (14)$$

An illustration of the bipartition of the  $\tau$  spins is shown in the inset-(b) of Fig. 5, where the shadow on part  $B$

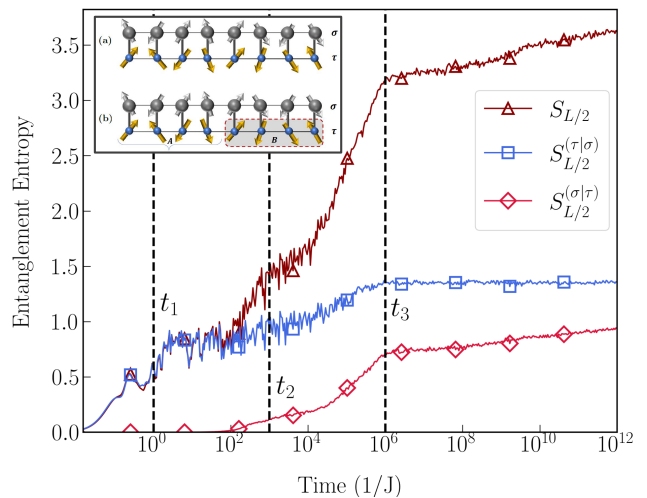


FIG. 5. (Color online) **(Inset)** Schematic representation of the procedure used to evaluate the measured entanglement entropy. (a) A projective measurement is performed on the  $\sigma$  spins (upper leg) of a many-body eigenstate, resulting in the collapse of the wavefunction to a configuration-dependent post-measurement state  $|\psi_p^{(m)}\rangle$  of the  $\tau$  spins. (b) For each measurement outcome, the half-cut entanglement entropy associated with subsystem  $A$  is computed as explained in the main text. **(Main)** Comparison of full and measured entanglement entropies in a spin ladder with strong inter-leg coupling  $J_z = 10$ . The total bipartite entropy  $S_{L/2}$  (dark-red triangles) displays three characteristic regimes as mentioned in Fig. 2. Measured entropies after projective measurements on one leg,  $S_A^{(\tau|\sigma)}$  (blue squares) and  $S_A^{(\sigma|\tau)}$  (red diamonds), reveal the asymmetry in thermalization between legs. Notably,  $S_A^{(\tau|\sigma)}$  saturates early, reflecting thermalization within the  $\tau$ , while  $S_A^{(\sigma|\tau)}$  remains strongly suppressed, indicating localization of the  $\sigma$ .

means the trace operation. The entanglement entropy of region  $A$  for the  $j$ -th configuration is given by

$$S_A^{(m,j)} = -\text{tr} \left[ \rho_A^{(m,j)} \log \rho_A^{(m,j)} \right]. \quad (15)$$

Finally, the full measured entanglement entropy of eigenstate  $|\psi^{(m)}\rangle$  is obtained by averaging over all measurement outcomes on the  $\sigma$  spins:

$$S_A^{(\tau|\sigma)}(m) = \sum_j P_j^{(m)} S_A^{(m,j)}. \quad (16)$$

This diagnostic captures the residual entanglement within the  $\tau$  spins after performing projective measurements on the  $\sigma$  spins. In thermal (ETH) eigenstates,  $S_A^{(\tau|\sigma)}$  remains volume-law, whereas in QDL regimes it drops significantly, indicating localization of lighter species and suppressed entanglement transfer across the legs. That means  $S_A^{(\tau|\sigma)}$  shows an area-law or sub-volume law in the QDL phase, indicating the localization of fast  $\tau$  degrees of freedom on the slow  $\sigma$  partners.

The procedure is repeated by exchanging the  $\sigma \leftrightarrow \tau$  spins in the above approach. That means the measure-

ment on  $\tau$  degree of freedom and obtaining the bipartite entanglement of the  $\sigma$  chain, which results in  $S_A^{(\sigma|\tau)}$ .

We present in Fig. 5 the time evolution of the entanglement entropy  $S_{L/2}$  for a ladder system with  $L = 8$  rungs at strong coupling ( $J_z = 10$ ). For times  $t > t_3$ ,  $S_{L/2}$  exhibits a clear logarithmic growth, indicative of quasi-MBL behavior (the same as shown in Fig. 2).

In addition to  $S_{L/2}$ , we compute the measured entropies as previously defined. The entropy of  $\tau$  spins conditioned on measured configurations of  $\sigma$  spins, denoted by  $S_A^{(\tau|\sigma)}$ , is shown in blue with square markers. This entropy follows a similar temporal profile to  $S_{L/2}$  up to  $t_2$ , and for  $t > t_2$  displaying logarithmic growth and rapid saturation at  $t_3$ . This behavior suggests that the light species (i.e.,  $\tau$  spins) thermalizes quickly and does not retain memory of observables, contrary to the expectations of the QDL paradigm (see Appendix B).

Conversely, the entropy of  $\sigma$  spins conditioned on measured  $\tau$  configurations,  $S_A^{(\sigma|\tau)}$ , remains nearly frozen for  $t < t_2$ , reflecting extremely slow dynamics in this regime. Between  $t_2$  and  $t_3$ ,  $S_A^{(\sigma|\tau)}$  increases rapidly, followed by an unbounded slow logarithmic growth for  $t > t_3$ . This evolution is responsible for the quasi-MBL behavior observed in  $S_{L/2}$ .

To further examine the contributions of  $\tau$  and  $\sigma$  spins to the entanglement dynamics of the model, we analyze the scaling behavior of the measured entropies of eigenstates with respect to subsystem size. As a first step, we plot the entanglement spectrum  $S_{L/2}^{(\tau|\sigma)}$  as a function of energy per rung,  $E/L$ , in Fig. 6(a).

Limited by available computational resources, we work at fixed magnetizations using PBC and exploit discrete symmetries of the ladder—lattice translation  $\hat{T}$  and leg parity  $\hat{P}$ , i.e.  $(S_\tau^z, S_\sigma^z, k, \mathcal{P}) = (0, 0, 0, +1)$ . The calculations are performed on a ladder system of length  $L = 10$ . Projecting onto these sectors block-diagonalizes the Hamiltonian and greatly reduces the effective Hilbert spaces. Within each block we compute, for all eigenstates available, the measured entropy of the light leg,  $S_{L/2}^{(\tau|\sigma)}$ , and display it against the energy density  $E/L$  in Fig. 6(a) (An analogous plot for the heavy leg,  $S_{L/2}^{(\sigma|\tau)}$ , displays the same band segmentation and is omitted). Four dominant bands are clearly resolved; two narrow edge bands exist but are not analyzed further.

For the scaling analysis in panels (b,c) we *do not* impose symmetry resolution in order to observe the generic behavior: instead, we target narrow spectral windows centered in the middle-right and right bands (starred regions in panel (a)) using a shift-and-invert method on the full (imposing  $S_\tau^z = S_\sigma^z = 0$ ) Hilbert space. From each band, we sample the central 20% of eigenstates (by energy), evaluate the measured entropies  $S_{L_A}^{(\tau|\sigma)}$  (blue, upper curves) and  $S_{L_A}^{(\sigma|\tau)}$  (red, lower curves) for subsystems of length  $L_A$ , and report the band averages as functions of  $L_A$  in Figs. 6(b)–(c). In both panels,  $S_{L_A}^{(\sigma|\tau)}$  exhibits sub-

volume scaling,  $S_{L_A}^{(\tau|\sigma)}$  displays significantly larger values and a stronger dependence on  $L_A$ , indicative of volume-law scaling. The left bands in Fig. 6–(a) are related to the right bands by symmetry and therefore exhibit identical behavior; they are omitted for brevity.

These observations are consistent with previous diagnostics: the  $\sigma$  spins exhibit slow thermalization, retaining memory and gradually saturating their entropy in a logarithmic-in-time fashion. Meanwhile, the  $\tau$  spins thermalize rapidly, as evidenced by their volume-law scaling of entanglement entropy.

We therefore conclude that the observed slow logarithmic growth of entanglement at  $t > t_3$  cannot be attributed to the standard QDL mechanism. Instead, it resembles a reversed-QDL phase. In the following section, we argue that this behavior originates from the emergence of local integrals of motion in the strong coupling limit ( $J_z \gg 1$ ) of the model.

## B. Emergent XXZ Dynamics in the strong coupling limit

To capture the rich physics of the strongly coupled ladder in the regime  $J_z \gg J, J'$ , we derive effective Hamiltonians for both the **low-energy** and **high-energy** subspaces. These correspond to two mutually orthogonal doublets localized on each rung of the ladder, with each doublet comprising a pair of degenerate eigenstates of the corresponding rung Hamiltonian.

*Low-energy effective theory*—We begin by projecting the full Hamiltonian onto the lower-energy doublet states of all rungs  $\{|\gamma_l^+\rangle, |\gamma_l^-\rangle; l = 1, \dots, L\}$ , which define an emergent spin- $\frac{1}{2}$  degree of freedom per rung. The corresponding Pauli operators  $\Gamma_l^\alpha$  ( $\alpha = x, y, z$ ) obey the standard algebra and act within this subspace.

The first-order contribution vanishes due to orthogonality with the excited sector, so we proceed with second-order Brillouin–Wigner perturbation theory [60–65]. The resulting effective Hamiltonian is (for details see Appendix C):

$$\mathcal{H}_{\text{eff}}^{(\text{low})} = -\frac{2JJ'}{J_z} \sum_{l=1}^L (\Gamma_l^x \Gamma_{l+1}^x + \Gamma_l^y \Gamma_{l+1}^y) + \left(\frac{J^2 + J'^2}{J_z}\right) \sum_{l=1}^L \Gamma_l^z \Gamma_{l+1}^z - \left(\frac{J^2 + J'^2}{J_z}\right) \mathbb{1}. \quad (17)$$

This Hamiltonian describes an effective XXZ spin chain, where transverse couplings arise from flip-flop processes and the longitudinal interaction originates from virtual excursions into the excited subspace. The final constant term induces a uniform shift in energy. The anisotropy parameter of the Heisenberg spin chain, defined as the ratio between the longitudinal ( $zz$ ) and transverse ( $xy$ ) coupling terms, satisfies the condition

$$\Delta = \frac{J^2 + J'^2}{2JJ'} \geq 1. \quad (18)$$

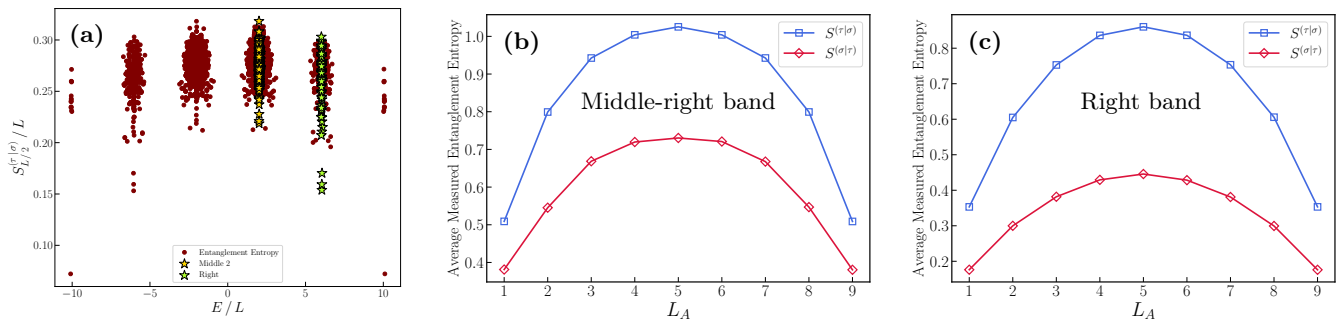


FIG. 6. (Color online) (a) Energy-resolved measured entanglement entropy normalized by system size,  $S_{L/2}^{(\tau|\sigma)}/L$ , versus energy density  $E/L$  for a ladder of length  $L = 10$ . (b, c) Scaling of measured entropies  $S_{L_A}^{(\tau|\sigma)}$  (blue, upper) and  $S_{L_A}^{(\sigma|\tau)}$  (red, lower) with subsystem size  $L_A$  for states in the middle-right and right bands, respectively. The  $\tau$  spins exhibit near volume-law behavior, indicating rapid thermalization, while  $\sigma$  spins show sub-volume scaling as a quasi-MBL phase.

This inequality places the system in the Ising regime, where the model remains integrable.

*High-energy effective theory*—The high-energy subspace is spanned by the excited doublets of rungs  $\{|\varphi_l^+\rangle, |\varphi_l^-\rangle; l = 1, \dots, L\}$ . Defining a new set of pseudospin operators  $\hat{\Phi}_l^\alpha$  within this subspace:

$$\begin{aligned}\hat{\Phi}_l^+ &= |\varphi_l^+\rangle \langle \varphi_l^-|, \\ \hat{\Phi}_l^- &= |\varphi_l^-\rangle \langle \varphi_l^+|, \\ \hat{\Phi}_l^z &= |\varphi_l^+\rangle \langle \varphi_l^+| - |\varphi_l^-\rangle \langle \varphi_l^-|. \end{aligned} \quad (19)$$

We again apply the second-order Brillouin–Wigner perturbation theory, yielding the effective Hamiltonian:

$$\begin{aligned}\mathcal{H}_{\text{eff}}^{(\text{high})} &= \frac{2JJ'}{J_z} \sum_{l=1}^L \left( \hat{\Phi}_l^x \hat{\Phi}_{l+1}^x + \hat{\Phi}_l^y \hat{\Phi}_{l+1}^y \right) \\ &\quad - \left( \frac{J^2 + J'^2}{J_z} \right) \sum_{l=1}^L \hat{\Phi}_l^z \hat{\Phi}_{l+1}^z + \frac{J^2 + J'^2}{J_z} \mathbb{1}. \end{aligned} \quad (20)$$

This sector also realizes an XXZ-type chain, but with **opposite sign** in the longitudinal interaction, reflecting its distinct spectral origin. The positive constant term shifts the high-energy manifold upward. Together, the two effective theories offer a complete picture of emergent spin dynamics across energy scales in the ladder system. The anisotropy of the high-energy effective Heisenberg chain satisfies Eq. 18, which puts the system into Ising regime.

The energy separation between the two doublets is given by  $2J_z$ , rendering them energetically well-separated in the strong coupling regime. In this limit, the effective theory of the spin ladder indicates that the Hilbert space decomposes into two dynamically disconnected sectors. Each sector is effectively described by an integrable spin- $\frac{1}{2}$  Heisenberg chain with anisotropy  $\Delta > 1$ , placing the system within the Ising regime. Consequently, for  $J_z \gg J, J'$ , the full model admits a description in terms

of emergent constants of motion associated with the integrable Heisenberg chains. This structure provides a natural interpretation of the quasi-MBL behavior observed at large  $J_z$ , where the local integrals of motion originate from the underlying integrability of the effective chains.

## VI. SUMMARY AND CONCLUSIONS

In this work, we have investigated the long-time dynamics of the two-leg spin- $\frac{1}{2}$  ladder introduced in [26], consisting of asymmetric XY interactions along the legs ( $J \gg J'$ ) and an Ising interaction on the rungs (coupling  $J_z$ ). Our results demonstrate that the dynamical behavior of the system is highly sensitive to  $J_z$ , giving rise to the phase diagram presented in Fig. 7. At  $J_z = 0$ , the system decouples into two independent spin- $\frac{1}{2}$  XY chains, which are integrable and exhibit the characteristic features of integrable models. The density of states (DoS) in this limit consists of two identical contributions with distinct energy scales reflecting the leg asymmetry ( $J = 1, J' = 0.001$ ). Introducing a finite rung coupling  $J_z$  induces interactions between the chains and drives the system into a chaotic regime. This transition manifests itself through the broadening of the density of states (DoS) and the emergence of statistical features consistent with the eigenstate thermalization hypothesis (ETH). This regime is characterized by rapid growth of the half-cut entanglement entropy toward its saturation value following a volume-law scaling, exponential growth of the rescaled adiabatic gauge potential norm with system size, and level statistics approaching the Gaussian orthogonal ensemble (GOE) limit. The corresponding DoS evolves into a compact distribution, as illustrated in Fig. 7 for  $J_z = 0.01$ . The chaotic phase persists up to a critical coupling  $J_z^c$ .

At the critical rung coupling  $J_z = J_z^c$ , the system undergoes a dynamical crossover to a reversed-QDL regime. Numerical results place the value of  $J_z^c \approx 1.0$ , as inferred from several diagnostics: a pronounced peak in fidelity

susceptibility, a crossover in level statistics from GOE to Poisson, a reduction of eigenstate entropies, and a change in the scaling of the rescaled AGP norm with system size. The DoS at the crossover displays a compact profile, consistent with critical behavior. Due to strong finite-size effects and the exponential growth of Hilbert space dimension with ladder length, we were limited to ladders of length  $L = 12$  ( $N = 24$  spins). For smaller sizes ( $L < 10$ ), level statistics remain below the Poisson limit for almost all  $J_z$ , highlighting the need for larger system sizes to establish scaling behavior with higher precision.

For strong couplings ( $J_z \gg 1$ ), the system exhibits a reversed-QDL regime, as evidenced by logarithmic growth of the entanglement entropy, super-linear scaling of the rescaled AGP norm with system size, and Poissonian level statistics. To explore the underlying mechanism, we examined the QDL scenario. In the highly asymmetric limit ( $J' \ll J$ ), the upper and lower legs may be regarded as slow and fast fermionic modes, respectively. While the standard QDL picture suggests thermalization of the slow modes and localization of the fast ones, our analysis reveals the opposite: the upper spins (slow fermions) remain localized, while the lower spins thermalize rapidly. This reversed-QDL behavior is reflected in the measurement-based entanglement entropy, which shows logarithmic growth of the upper-spin entropy when conditioned on lower-spin measurements (Fig. 5). Furthermore, a second-order effective Hamiltonian in the strong-coupling regime reduces to two decoupled spin- $\frac{1}{2}$  Heisenberg chains with spectra separated by  $\Delta E = 2J_z \gg 1$ . This spectral fragmentation, evident in the DoS at  $J_z = 10$  (Fig. 7), provides a natural source of local integrals of motion stabilizing the quasi-MBL phase.

Finally, we emphasize that the asymmetry of the leg couplings plays a crucial role. At  $J_z = 10$ , increasing  $J'$  toward  $J$  leads to rapid growth of the entanglement entropy and restores thermalization, even in the strong-coupling regime. This confirms that the imbalance between the legs is essential for sustaining the quasi-MBL behavior. Taken together, these results establish a rich dynamical phase structure for the two-leg spin- $\frac{1}{2}$  ladder: an integrable regime at  $J_z = 0$ , a chaotic thermal phase for  $0 < J_z < J_z^c$ , and a quasi-MBL regime for  $J_z \gtrsim J_z^c$ , with the strong-coupling limit exhibiting reversed-QDL behavior and spectral fragmentation.

The ladder Hamiltonian exhibits extensive symmetries—most notably conservation of magnetization on each leg, translation invariance, and spin-inversion symmetry—which necessitate working in carefully resolved subspaces. Additionally, the presence of two markedly distinct energy scales in our model induces significant finite-size effects, making it challenging to extrapolate numerical results from small systems to the thermodynamic limit [66]. Moreover, the exponential growth of the Hilbert space dimension restricts us to system sizes up to  $L = 12$ , which, although sufficient to expose clear dynamical trends, leaves open the question of scaling to the thermodynamic limit.

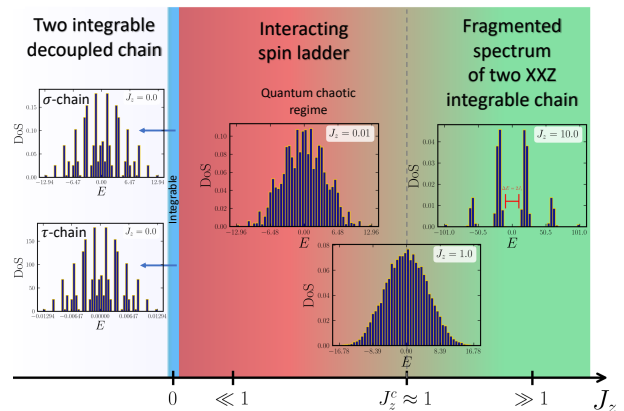


FIG. 7. (Color online) Phase diagram of the spin ladder as a function of the inter-leg Ising coupling  $J_z$ . For  $J_z = 0$ , the system consists of two decoupled integrable chains (blue region), each exhibiting a discrete and regular spectrum. As  $J_z$  increases ( $J_z \ll 1$ ), the inter-leg interactions induce chaotic dynamics, leading to a quantum chaotic regime (red region). Notably, the density of states for small  $J_z$  (e.g.,  $J_z = 0.01$ ) actually signals the onset of coupling between the two chains, giving rise to quantum ergodicity and ETH-like behavior. Around the crossover scale  $J_z^c \sim 1$ , the density of states (DoS) becomes fully broadened and ergodic. For  $J_z \gg 1$ , the ladder effectively reduces to two weakly coupled XXZ chains in the strong coupling limit (green region), exhibiting a fragmented spectrum arising from the emergent effective theory derived in Sec. VB. The spectrum consists of a series of subbands, each separated by an energy gap of  $\Delta E = 2J_z \gg 1$ . Inset plots show representative DoS for selected values of  $J_z$ .

In summary, we demonstrate a reentrant transition with increasing  $J_z$ : from an integrable nonergodic regime, through a chaotic thermalizing phase, and into a robust nonthermal regime at strong coupling. The latter hosts a reversed QDL structure, where the light species thermalizes while the heavy one remains localized, establishing a disorder-free mechanism for localization driven by inter-sector entanglement asymmetry. Our results thus provide a minimal microscopic route to interaction-induced nonergodicity, with implications for constrained dynamics, quantum simulators, and the broader taxonomy of nonthermal quantum matter.

## ACKNOWLEDGMENTS

This work was supported by the Iran National Science Foundation (INSF) under Grant No. 4037050. The authors thank Hyeongjin Kim for sharing helpful material. Special thank is devoted to H. Yarloo for the careful reading of the manuscript, fruitful discussions and useful comments. Part of the numerical computations was performed using the QuSpin library [67, 68].

## Appendix A: Level spacing statistics

We compute the mean level-spacing ratio to distinguish between integrable (non-thermal) and chaotic (thermal) regimes [6, 46]. All numerical exact diagonalizations are performed in the symmetry-resolved sector ( $\mathcal{S}_\tau^z = 0, \mathcal{S}_\sigma^z = 0, k, \mathcal{Z}$ ). For  $L = 10$  all sixteen symmetry sectors are considered, while for  $L = 12$  six symmetry sectors  $(0, 0, \pi/6, \pm 1)$ ,  $(0, 0, 5\pi/6, \pm 1)$  and  $(0, 0, 11\pi/6, \pm 1)$  are taken into account. To avoid the edge effects we restrict the computations to the 50% of the levels in the centre of spectrum for both  $L = 10$  and  $L = 12$ .

The mean ratio is defined as

$$r_n = \frac{\min(\delta_n, \delta_{n+1})}{\max(\delta_n, \delta_{n+1})}, \quad (\text{A1})$$

where  $\delta_n = E_{n+1} - E_n$  denotes the spacing between consecutive energy levels. A key advantage of the  $r$ -statistic is that it does not require spectral unfolding, which makes it particularly robust in finite-size systems. The ensemble average  $\langle r \rangle$  approaches  $\approx 0.531$  for Wigner–Dyson (chaotic) statistics and  $\approx 0.387$  for Poisson (integrable) statistics [46].

Figure 8 shows the average ratio  $\langle r \rangle$  as a function of  $J_z$  for system sizes  $L = 10$  and  $L = 12$ . At  $J_z = 0$ , the model reduces to two decoupled integrable spin- $\frac{1}{2}$  XY chains, yielding the Poissonian value of  $\langle r \rangle$ . Increasing  $J_z$  induces a dynamical transition into a chaotic phase, where  $\langle r \rangle$  approaches the Gaussian Orthogonal Ensemble (GOE) value. For both  $L = 10$  and  $L = 12$ , the data clearly exhibit a sharp transition from the Poissonian limit to the GOE regime as  $J_z$  is increased.

As  $J_z$  increases further, the mean level-spacing ratio  $\langle r \rangle$  decreases again toward the Poisson value around  $J_z \simeq 1$ . This trend is consistent with other diagnostics indicating that a dynamical crossover back to Poisson-like statistics occurs at large  $J_z$ , signaling MBL-like behavior in this regime.

It is important to note that the system under study is quasi-1D (a two-leg ladder). Consequently, extending calculations beyond  $L = 12$  (corresponding to more than 24 spins) requires computational resources beyond typical availability. Additionally, results for smaller system sizes ( $L < 10$ ) are not presented due to pronounced finite-size effects although confirm the qualitative behavior.

## Appendix B: Scaling fits as evidence for a reversed QDL regime

To diagnose scaling in our two-leg ladder, we analyze the long-time saturation values of the *measured* half-cut entanglement entropy  $S_{L/2}^{(\beta)}(t)$  at system sizes  $L = 4, 6, 8$ , with  $\beta \in \{\tau|\sigma, \sigma|\tau\}$ .

For each system size  $L$  we record the time series  $S_{L/2}^{(\beta)}(t)$  at discrete sampling times  $t_1, \dots, t_{M_L}$ , where  $M_L$  is the number of time samples.

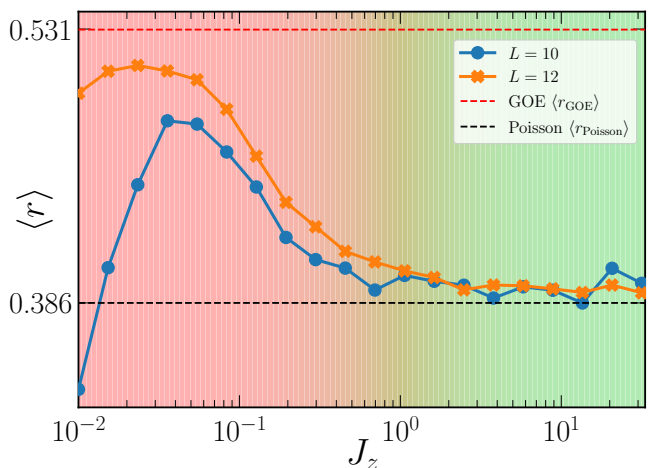


FIG. 8. (Color online) Average adjacent level-spacing ratio  $\langle r \rangle$  as a function of  $J_z$  for system sizes  $L = 10$  and  $L = 12$ . Increasing  $J_z$  induces a crossover around  $J_z \simeq 1$  from GOE (chaotic) to Poisson statistics. See the main text for the details.

We estimate the long-time *saturation values* by averaging over the last fraction of this record:

- Choose a tail fraction  $f$  (we use  $f = 0.2$ ).
- Let  $K_L = \lfloor f M_L \rfloor$  be the number of samples in the tail.
- Define the tail (terminal) index set  $\mathcal{I}_{\text{tail}}(L) = \{M_L - K_L + 1, \dots, M_L\}$ , i.e., the last  $K_L$  points of the record.

The saturation value is then the mean of those last  $K_L$  samples:

$$S_{\text{sat}}^{(\beta)}(L) = \frac{1}{K_L} \sum_{k \in \mathcal{I}_{\text{tail}}(L)} S_{L/2}^{(\beta)}(t_k). \quad (\text{B1})$$

Its error bar reflects the scatter within that tail window. We report the standard error of the mean (SEM),

$$\text{SEM}(L) = \frac{s(L)}{\sqrt{K_L}}, \quad s(L)^2 = \frac{1}{K_L - 1} \sum_{k \in \mathcal{I}_{\text{tail}}(L)} [S_{L/2}^{(\beta)}(t_k) - S_{\text{sat}}^{(\beta)}(L)]^2. \quad (\text{B2})$$

We then fit the saturation values by (weighted) least squares to three size-scaling ansätze:

$$\text{linear: } S_{\text{sat}}(L) = aL + b, \quad (\text{B3})$$

$$\text{power law: } S_{\text{sat}}(L) = aL^\alpha + b, \quad (\text{B4})$$

$$\text{logarithmic: } S_{\text{sat}}(L) = c \log L + d. \quad (\text{B5})$$

When SEM estimates are available, each datum is weighted by  $w_i = \text{SEM}(L_i)^{-2}$ . We report the coefficient of determination  $R^2$  for goodness of fit, but model preference is established using out-of-sample and information-theoretic criteria: residual sum of squares (RSS),

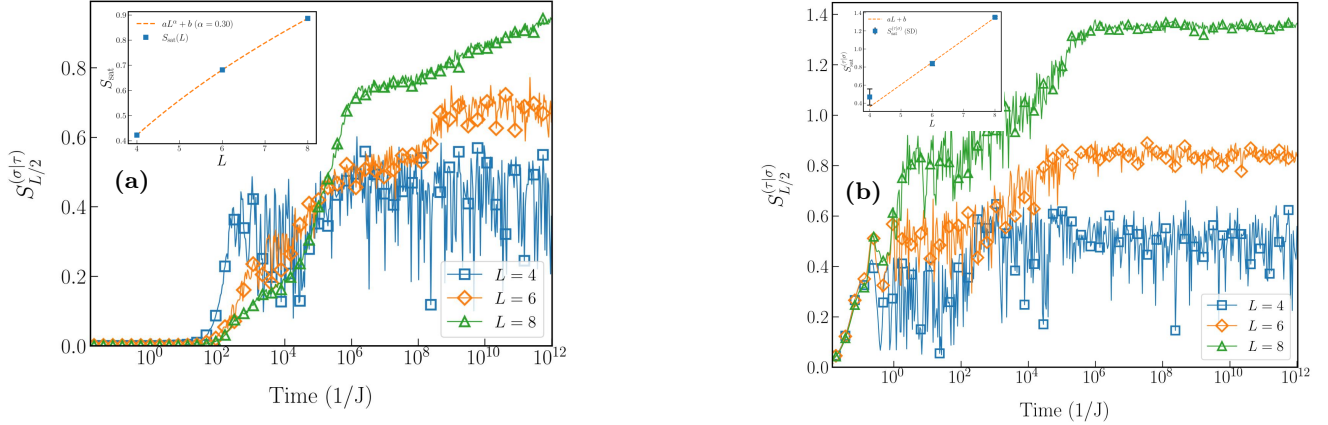


FIG. 9. (Color online) (a) **Heavy leg ( $\sigma$ )—measured half-cut entanglement entropy.** Main panel show  $S_{L/2}^{(\sigma|\tau)}(t)$ ; the inset reports the terminal-window saturation values  $S_{\text{sat}}^{(\sigma|\tau)}(L)$  together with the best *power-law* fit  $S_{\text{sat}}(L) = aL^\alpha + b$  with  $\alpha \simeq 0.30$ , indicating sub-volume growth. (b) **Light leg ( $\tau$ )—measured half-cut entanglement entropy.** Main panel show  $S_{L/2}^{(\tau|\sigma)}(t)$ ; the inset shows  $S_{\text{sat}}^{(\tau|\sigma)}(L)$  with the best *linear* fit  $S_{\text{sat}}(L) = aL + b$ , consistent with volume-law scaling, where *error bars* display the one-standard-deviation spread of the terminal window used to define  $S_{\text{sat}}$ . In both panels results are shown for  $L = 4, 6, 8$  with periodic boundary conditions (PBC). The model parameters are  $J = 1$ ,  $J' = 10^{-3}$ ,  $J_z = 10$ , and all calculations are performed in the symmetry sector  $\mathcal{S}_z^z = \mathcal{S}_z^z = 0$  (i.e.,  $\mathcal{S}^z$  per leg = 0).

the small-sample-corrected Akaike information criterion AICc [69, 70] with Akaike weights [71], leave-one-out cross-validated MSE (LOO-CV) [72], and the Bayesian information criterion BIC [73]. Lower AICc/BIC and CV-MSE, together with smaller RSS (and larger  $R^2$ ), indicate the superior model.

*Heavy ( $\sigma$ ) leg — sub-volume scaling.* From the long-time saturation values [Fig. 9(a)], a two-parameter power law  $S_{\text{sat}}^{(\sigma|\tau)}(L) = aL^\alpha + b$  is decisively preferred by information-theoretic criteria over logarithmic and linear alternatives. Using BIC we find  $\text{BIC}_{\text{pow}} = -66.45$ ,  $\text{BIC}_{\text{log}} = -25.47$ , and  $\text{BIC}_{\text{lin}} = -20.61$  (with comparable parameter counts), while the fits have  $R_{\text{pow}}^2 = 1.000$  vs.  $R_{\text{log}}^2 = 0.997$  and residual sums of squares  $\text{RSS}_{\text{pow}} = 3.47 \times 10^{-10}$  vs.  $\text{RSS}_{\text{log}} = 2.97 \times 10^{-4}$ . Leave-one-out CV-MSE is slightly smaller for the logarithmic fit ( $4.53 \times 10^{-4}$  vs.  $7.30 \times 10^{-4}$ ), but the BIC differences in favor of the power law are decisive:  $\Delta\text{BIC}_{\text{pow,log}} \sim 41$ . The best fit yields  $\alpha \simeq 0.30$  (robust across tail windows,  $\alpha \in [0.22, 0.48]$ ), establishing *sub-volume* growth of the measured entropy in the heavy sector (see Table I).

*Light ( $\tau$ ) leg — volume-law scaling.* For the light leg [Fig. 9(b)], model selection based on BIC gives a tie between a linear and a power-law fit (both  $\text{BIC} = -14.283$ ), while leave-one-out CV-MSE favors the linear model (linear =  $1.532 \times 10^{-2}$  vs. power =  $2.457 \times 10^{-2}$ ). A linear fit  $S_{\text{sat}}^{(\tau|\sigma)}(L) = aL + b$  yields  $a = 0.247876$  with a 95% CI [0.245651, 0.250183] and  $b = -0.633417$ . The best power-law fit returns  $\alpha \simeq 1$ , indistinguishable from linear by BIC, confirming extensive (thermal) *volume-law* scaling  $S_{\text{sat}}^{(\tau|\sigma)} \propto L$  for the measured entropy in the light

sector (see Table I).

*Reversed QDL.* In the canonical QDL scenario [22], the heavy degrees of freedom thermalize and, *after measuring the heavy species*, the remaining (“disentangled”) species exhibits an *area law* for the measured entanglement (in 1D,  $S = \mathcal{O}(1)$ ). In finite-size, dynamical settings this can appear as weaker *sub-volume* growth (e.g.,  $S \sim L^\alpha$  with  $0 < \alpha < 1$ ). In our ladder the *measured* entropy shows the *opposite* hierarchy:

- Light ( $\tau$ ) spins:  $S_{\text{sat}}^{(\tau|\sigma)}(L) \propto L$  (volume law; thermal).
- Heavy ( $\sigma$ ) spins:  $S_{\text{sat}}^{(\sigma|\tau)}(L) \propto L^\alpha$  with  $\alpha < 1$  (sub-volume; localized). Our best fit gives  $\alpha \simeq 0.30$  (robust across analysis windows), decisively favored over linear and logarithmic alternatives by BIC, with small RSS and competitive CV-MSE.

*Remark on admissible scalings.* Our system is a fixed-width (quasi-1D) ladder, so the relevant “volume” scales as  $V \sim WL$  with constant width  $W = 2$ . Locality and Page-like bounds imply  $S(A) \leq \ln(\dim \mathcal{H}_A) = (WL) \ln 2$ , hence  $S_{\text{sat}} = \mathcal{O}(L)$ . Although a two-parameter power law can occasionally favor an exponent  $\alpha > 1$  on three sizes, such super-linear fits are super-extensive and unreliable for extrapolation; we therefore restrict to  $\alpha \leq 1$ . For the light leg this collapses to  $\alpha \simeq 1$  (volume law), while the heavy leg exhibits genuine sub-volume scaling with  $\alpha < 1$ .

TABLE I. Saturation values of the *measured* entropy  $S_{\text{sat}}(L)$  with SEM uncertainties, best model, and inferred scaling.

Sector	$L$	$S_{\text{sat}} \pm \text{SEM}$	Best fit	Scaling
	4	$0.422503 \pm 0.010370$	power	
$\sigma$ (heavy)	6	$0.681881 \pm 0.003113$	$(\alpha \simeq 0.30)$	sub-volume
	8	$0.886123 \pm 0.003142$		
	4	$0.468061 \pm 0.008992$		
$\tau$ (light)	6	$0.838122 \pm 0.002404$	linear	volume
	8	$1.351117 \pm 0.001058$		

### Appendix C: Effective Two-Rung Theory in the Strong Coupling Limit

To develop an effective theory in the strong coupling limit  $J_z \gg J, J'$ , we begin by analyzing the Hamiltonian for a pair of neighboring rungs  $\ell, \ell + 1$ . The full spin ladder consists of two chains: one made of  $\sigma$ -spins (upper leg) and the other of  $\tau$ -spins (lower leg), both being spin- $\frac{1}{2}$  degrees of freedom Fig. 10.

The leading contribution to the rung interaction is encapsulated by the unperturbed Hamiltonian

$$H_0 = \frac{J_z}{2} \sum_{\ell=1}^2 \tau_{\ell}^z \sigma_{\ell}^z, \quad (\text{C1})$$

where the prefactor  $J_z/2$  represents the interaction strength *per rung*. Since each rung contains a single  $\tau^z \sigma^z$  interaction, the total energy per pair of rungs would scale with  $J_z$ , and thus we include the factor of 1/2 to avoid overcounting when generalizing to the full ladder denoted by  $H_{zz}$  in Eq. 1

The eigenstates of  $H_0$  on each rung organize into two energy-separated doublets:

$$|\gamma_{\ell}^+\rangle = |\downarrow\rangle_{\tau} \otimes |\uparrow\rangle_{\sigma}, \quad |\gamma_{\ell}^-\rangle = |\uparrow\rangle_{\tau} \otimes |\downarrow\rangle_{\sigma}, \quad (\text{C2})$$

$$|\varphi_{\ell}^+\rangle = |\uparrow\rangle_{\tau} \otimes |\uparrow\rangle_{\sigma}, \quad |\varphi_{\ell}^-\rangle = |\downarrow\rangle_{\tau} \otimes |\downarrow\rangle_{\sigma}. \quad (\text{C3})$$

The states  $|\gamma_{\ell}^{\pm}\rangle$  span the low-energy sector with energy  $-J_z$ , while the  $|\varphi_{\ell}^{\pm}\rangle$  reside in the high-energy sector with energy  $+J_z$ .

Within the doublet subspace  $\{|\gamma_i^{\pm}\rangle\}$ , we define pseudospin operators:

$$\begin{aligned} \hat{\Gamma}_i^+ &= |\gamma_i^+\rangle \langle \gamma_i^-|, \\ \hat{\Gamma}_i^- &= |\gamma_i^-\rangle \langle \gamma_i^+|, \\ \hat{\Gamma}_i^z &= |\gamma_i^+\rangle \langle \gamma_i^+| - |\gamma_i^-\rangle \langle \gamma_i^-|. \end{aligned} \quad (\text{C4})$$

We introduce the perturbing terms:

$$V_1 = 2J (\tau_{\ell}^+ \tau_{\ell+1}^- + \tau_{\ell}^- \tau_{\ell+1}^+), \quad (\text{C5})$$

$$V_2 = 2J' (\sigma_{\ell}^+ \sigma_{\ell+1}^- + \sigma_{\ell}^- \sigma_{\ell+1}^+), \quad (\text{C6})$$

with total perturbation  $V = V_1 + V_2$ .

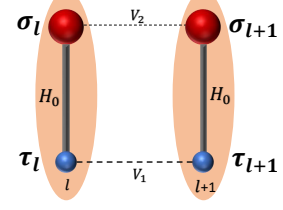


FIG. 10. (Color online) Schematic of two rungs of the spin ladder. The dominant rung coupling  $H_0$  (solid lines) defines the unperturbed Hamiltonian, while the leg couplings  $V_1$  and  $V_2$  (dashed lines) are treated perturbatively. Each rung hosts a pair of coupled spins ( $\tau_i, \sigma_i$ ), forming the basis for the effective low- and high-energy subspaces.

The spectral decomposition of  $H_0$  implies a two-level structure and a clear energy gap of  $2J_z$ . Projecting onto the low-energy subspace using:

$$P = P_{\ell} \otimes P_{\ell+1}, \quad Q = \mathbb{1} - P, \quad (\text{C7})$$

$$P_{\ell} = \sum_{\pm} |\gamma_{\ell}^{\pm}\rangle \langle \gamma_{\ell}^{\pm}|, \quad Q_{\ell} = \sum_{\pm} |\varphi_{\ell}^{\pm}\rangle \langle \varphi_{\ell}^{\pm}|, \quad (\text{C8})$$

We compute the second-order contribution to the effective Hamiltonian using Brillouin–Wigner perturbation theory:

$$H_{\text{eff}}^{(\text{low})} = -\frac{1}{2J_z} P V Q V P. \quad (\text{C9})$$

Evaluating each term:

$$P V_1 Q V_1 P = 2J^2 (\mathbb{1} - \Gamma_{\ell}^z \Gamma_{\ell+1}^z), \quad (\text{C10})$$

$$P V_2 Q V_2 P = 2J'^2 (\mathbb{1} - \Gamma_{\ell}^z \Gamma_{\ell+1}^z), \quad (\text{C11})$$

$$P V_2 Q V_1 P = 2J J' (\Gamma_{\ell}^x \Gamma_{\ell+1}^x + \Gamma_{\ell}^y \Gamma_{\ell+1}^y), \quad (\text{C12})$$

$$P V_1 Q V_2 P = 2J J' (\Gamma_{\ell}^x \Gamma_{\ell+1}^x + \Gamma_{\ell}^y \Gamma_{\ell+1}^y), \quad (\text{C13})$$

the final effective Hamiltonian reads:

$$\begin{aligned} \mathcal{H}_{\text{eff}}^{(\text{low})} &= -\frac{2J J'}{J_z} (\Gamma_{\ell}^x \Gamma_{\ell+1}^x + \Gamma_{\ell}^y \Gamma_{\ell+1}^y) \\ &\quad + \left( \frac{J^2 + J'^2}{J_z} \right) \Gamma_{\ell}^z \Gamma_{\ell+1}^z - \left( \frac{J^2 + J'^2}{J_z} \right) \mathbb{1}. \end{aligned} \quad (\text{C14})$$

- 
- [1] J. M. Deutsch, *Phys. Rev. A* **43**, 2046 (1991).
- [2] M. Srednicki, *Phys. Rev. E* **50**, 888 (1994).
- [3] M. Rigol, V. Dunjko, and M. Olshanii, *Nature* **452**, 854–858 (2008).
- [4] L. D’Alessio, Y. Kafri, A. Polkovnikov, and M. Rigol, *Advances in Physics* **65**, 239–362 (2016).
- [5] D. Basko, I. Aleiner, and B. Altshuler, *Annals of Physics* **321**, 1126–1205 (2006).
- [6] V. Oganesyan and D. A. Huse, *Physical Review B* **75**, 10.1103/physrevb.75.155111 (2007).
- [7] R. Nandkishore and D. A. Huse, *Annual Review of Condensed Matter Physics* **6**, 15–38 (2015).
- [8] P. Sierant, M. Lewenstein, A. Scardicchio, L. Vidmar, and J. Zakrzewski, *Reports on Progress in Physics* **88**, 026502 (2025).
- [9] D. A. Abanin, E. Altman, I. Bloch, and M. Serbyn, *Rev. Mod. Phys.* **91**, 021001 (2019).
- [10] B. Buča, *Phys. Rev. X* **13**, 031013 (2023).
- [11] P. Sala, T. Rakovszky, R. Verresen, M. Knap, and F. Pollmann, *Physical Review X* **10**, 10.1103/physrevx.10.011047 (2020).
- [12] V. Khemani, M. Hermele, and R. Nandkishore, *Physical Review B* **101**, 10.1103/physrevb.101.174204 (2020).
- [13] J. Jeyaretnam, T. Bhore, J. J. Osborne, J. C. Halimeh, and Z. Papić, *Communications Physics* **8**, 10.1038/s42005-025-02039-8 (2025).
- [14] F. Yang, H. Yarloo, H.-C. Zhang, K. Mølmer, and A. E. B. Nielsen, *Physical Review B* **111**, 10.1103/physrevb.111.144313 (2025).
- [15] C. J. Turner, A. A. Michailidis, D. A. Abanin, M. Serbyn, and Z. Papić, *Nat. Phys.* **14**, 745 (2018).
- [16] M. Serbyn, D. A. Abanin, and Z. Papić, *Nature Physics* **17**, 675–685 (2021).
- [17] N. S. Srivatsa, H. Yarloo, R. Moessner, and A. E. B. Nielsen, *Physical Review B* **108**, 10.1103/physrevb.108.1100202 (2023).
- [18] H. Yarloo, H.-C. Zhang, and A. E. B. Nielsen, *PRX Quantum* **5**, 020365 (2024), [arXiv:2306.13967 \[quant-ph\]](https://arxiv.org/abs/2306.13967).
- [19] A. A. Michailidis, C. J. Turner, Z. Papić, D. A. Abanin, and M. Serbyn, *Phys. Rev. X* **10**, 011055 (2020).
- [20] E. van Nieuwenburg, Y. Baum, and G. Refael, *Proceedings of the National Academy of Sciences* **116**, 9269 (2019), <https://www.pnas.org/doi/pdf/10.1073/pnas.1819316116>.
- [21] M. Schulz, C. A. Hooley, R. Moessner, and F. Pollmann, *Phys. Rev. Lett.* **122**, 040606 (2019).
- [22] T. Grover and M. P. A. Fisher, *Journal of Statistical Mechanics: Theory and Experiment* **2014**, P10010 (2014).
- [23] T. Veness, F. H. L. Essler, and M. P. A. Fisher, *Physical Review B* **96**, 10.1103/physrevb.96.195153 (2017).
- [24] E. Abbasgholinejad, S. Raesi, and A. Langari, *Physica A: Statistical Mechanics and its Applications* **615**, 128561 (2023).
- [25] A. Smith, J. Knolle, R. Moessner, and D. Kovrizhin, *Physical Review Letters* **119**, 10.1103/physrevlett.119.176601 (2017).
- [26] N. Yao, C. Laumann, J. Cirac, M. Lukin, and J. Moore, *Physical Review Letters* **117**, 10.1103/physrevlett.117.240601 (2016).
- [27] H. Yarloo, A. Langari, and A. Vaezi, *Physical Review B* **97**, 10.1103/physrevb.97.054304 (2018).
- [28] P. Sala, G. Giudici, and J. C. Halimeh, *Physical Review B* **109**, 10.1103/physrevb.109.1060305 (2024).
- [29] K. G. S. H. Gunawardana and B. Uchoa, *Physical Review B* **110**, 10.1103/physrevb.110.054207 (2024).
- [30] Y. Kuno, T. Orito, and I. Ichinose, *New Journal of Physics* **22**, 013032 (2020).
- [31] T. Orito, Y. Kuno, and I. Ichinose, *Physical Review B* **103**, 10.1103/physrevb.103.1060301 (2021).
- [32] S. Moudgalya, B. A. Bernevig, and N. Regnault, *Reports on Progress in Physics* **85**, 086501 (2022).
- [33] A. Chandran, T. Iadecola, V. Khemani, and R. Moessner, *Annual Review of Condensed Matter Physics* **14**, 443 (2023).
- [34] V. Ros, M. Müller, and A. Scardicchio, *Nuclear Physics B* **891**, 420–465 (2015).
- [35] M. Serbyn, Z. Papić, and D. A. Abanin, *Physical Review Letters* **111**, 10.1103/physrevlett.111.127201 (2013).
- [36] J. H. Bardarson, F. Pollmann, and J. E. Moore, *Physical Review Letters* **109**, 10.1103/physrevlett.109.017202 (2012).
- [37] P. T. Dumitrescu, R. Vasseur, and A. C. Potter, *Physical Review Letters* **119**, 10.1103/physrevlett.119.110604 (2017).
- [38] S.-J. GU, *International Journal of Modern Physics B* **24**, 4371–4458 (2010).
- [39] D. Sels and A. Polkovnikov, *Physical Review E* **104**, 10.1103/physreve.104.054105 (2021).
- [40] H. Kim, C. Lim, K. Matirko, A. Polkovnikov, and M. O. Flynn, (2025), [arXiv:2401.01927 \[cond-mat.stat-mech\]](https://arxiv.org/abs/2401.01927).
- [41] R. Świątek, P. Łydzba, and L. Vidmar, *Phys. Rev. B* **111**, 184203 (2025).
- [42] M. Kolodrubetz, D. Sels, P. Mehta, and A. Polkovnikov, *Physics Reports* **697**, 1–87 (2017).
- [43] M. Pandey, P. W. Claeys, D. K. Campbell, A. Polkovnikov, and D. Sels, *Physical Review X* **10**, 10.1103/physrevx.10.041017 (2020).
- [44] T. LeBlond, D. Sels, A. Polkovnikov, and M. Rigol, *Physical Review B* **104**, 10.1103/physrevb.104.l201117 (2021).
- [45] H. Kim and A. Polkovnikov, *Physical Review B* **109**, 10.1103/physrevb.109.195162 (2024).
- [46] Y. Y. Atas, E. Bogomolny, O. Giraud, and G. Roux, *Physical Review Letters* **110**, 10.1103/physrevlett.110.084101 (2013).
- [47] L. F. Santos and M. Rigol, *Physical Review E* **81**, 10.1103/physreve.81.036206 (2010).
- [48] T. Giamarchi, *Quantum Physics in One Dimension* (Oxford University Press, 2003).
- [49] P. Jordan and E. Wigner, *Z. Phys.* **47**, 631 (1928).
- [50] E. Lieb, T. Schultz, and D. Mattis, *Ann. Phys.* **16**, 407 (1961).
- [51] P. W. Anderson, *Phys. Rev.* **109**, 1492 (1958).
- [52] V. Khemani, S. Lim, D. Sheng, and D. A. Huse, *Physical Review X* **7**, 10.1103/physrevx.7.021013 (2017).
- [53] L. Amico, R. Fazio, A. Osterloh, and V. Vedral, *Rev. Mod. Phys.* **80**, 517 (2008).
- [54] N. Laflorencie, *Physics Reports* **646**, 1–59 (2016).
- [55] W.-L. You, Y.-W. Li, and S.-J. Gu, *Physical Review E* **76**, 10.1103/physreve.76.022101 (2007).
- [56] D. Sels and A. Polkovnikov, *Phys. Rev. X* **13**, 011041 (2023).
- [57] D. Sels and A. Polkovnikov, *Proceedings of the National*

- Academy of Sciences **114**, [10.1073/pnas.1619826114](https://doi.org/10.1073/pnas.1619826114) (2017).
- [58] E. Bianchi, L. Hackl, M. Kieburg, M. Rigol, and L. Vidmar, *PRX Quantum* **3**, [10.1103/prxquantum.3.030201](https://doi.org/10.1103/prxquantum.3.030201) (2022).
- [59] D. Ben-Zion, J. McGreevy, and T. Grover, *Physical Review B* **101**, [10.1103/physrevb.101.115131](https://doi.org/10.1103/physrevb.101.115131) (2020).
- [60] C. Bloch, *Nuclear Physics* **6**, 329 (1958).
- [61] R. Winkler, *Spin-Orbit Coupling Effects in Two-Dimensional Electron and Hole Systems*, 1st ed., Springer Tracts in Modern Physics, Vol. 191 (Springer, Berlin, Heidelberg, 2003) pp. XII, 228.
- [62] S. Bravyi, D. P. DiVincenzo, and D. Loss, *Annals of Physics* **326**, 2793–2826 (2011).
- [63] A. H. MacDonald, S. M. Girvin, and D. Yoshioka, *Phys. Rev. B* **37**, 9753 (1988).
- [64] C. Cohen-Tannoudji, J. Dupont-Roc, and G. Grynberg, *Atom-Photon Interactions: Basic Processes and Applications* (Wiley, 1992).
- [65] I. Hubac and S. Wilson, *J. Phys. B: At. Mol. Opt. Phys.* **33**, 365 (2000).
- [66] Z. Papić, E. M. Stoudenmire, and D. A. Abanin, *Annals of Physics* **362**, 714–725 (2015).
- [67] P. Weinberg and M. Bukov, *SciPost Phys.* **2**, 003 (2017).
- [68] P. Weinberg and M. Bukov, *SciPost Phys.* **7**, 020 (2019).
- [69] H. Akaike, *IEEE Transactions on Automatic Control* **19**, 716 (1974).
- [70] C. M. HURVICH and C.-L. TSAI, *Biometrika* **76**, 297 (1989), <https://academic.oup.com/biomet/article-pdf/76/2/297/737009/76-2-297.pdf>.
- [71] K. P. Burnham and D. R. Anderson, *Model Selection and Multimodel Inference: A Practical Information-Theoretic Approach*, 2nd ed. (Springer, New York, NY, 2002) hardcover ISBN 978-0-387-95364-9 (2002); Softcover ISBN 978-1-4419-2973-0 (2010); eBook ISBN 978-0-387-22456-5 (2007).
- [72] M. Stone, *Journal of the Royal Statistical Society. Series B (Methodological)* **39**, 44 (1977).
- [73] G. Schwarz, *The Annals of Statistics* **6**, 461 (1978).